CLIMATE CHANGE IN SPACE: THERMOSPHERIC DENSITY REDUCTIONS IN LEO AND THE IMPACT ON THE DEBRIS ENVIRONMENT

M. K. Brown[(1)], **H. G. Lewis**[(1)], **A. J. Kavanagh**[(2)], **and I. Cnossen**[(2)]

[(1)]*University of Southampton, Faculty of Engineering and Physical Sciences, Boldrewood Innovation Campus, Southampton, SO16 7QF, United Kingdom, Email: {mkb1g12, H.G.Lewis}@soton.ac.uk*
[(2)]*British Antarctic Survey, High Cross, Madingley Road, Cambridge, CB3 0ET, United Kingdom*

ABSTRACT

Simulations of the thermosphere under increasing carbon dioxide concentrations have been performed with the Whole Atmosphere Community Climate Model - extended (WACCM-X). These have been used to create a density scaling factor for thermospheric density, which is dependent upon altitude, ground-level carbon dioxide (CO_2) concentration, and solar activity. Results show there has already been a 21% decrease in thermospheric density at 400 km altitude since the year 2000. If global temperatures increase by $1.5°C$, WACCM-X predicts there will be a 15-32% decrease in density at 400 km compared to the year 2000 (dependent upon solar activity). Moreover, the reduction in thermospheric density is predicted to continue at higher rates with further increases in the ground level CO_2 concentration. The debris environment has been modelled with the new debris model, BRAD. It is shown how the number of trackable objects up to 500 km increases at a faster rate under increasing CO_2 concentrations, specifically following four Representative Concentration Pathways for CO_2 concentration through to the year 2100. Even under a best-case scenario of low CO_2 emissions, the population growth rate doubles. Further emissions lead to even larger population growth rates. Furthermore, high CO_2 concentrations lead to diminishing densities during solar maximum so fewer objects decay from LEO before the following solar minimum.

Keywords: Carbon Dioxide; Climate Change; Debris Model; Density; Drag; LEO; Solar Activity.

1. INTRODUCTION

While carbon dioxide (CO_2) causes global warming in the lower atmosphere (below 30 km), it causes the opposite effect at higher levels within the atmosphere, named global cooling [26]. The CO_2 molecules can gain energy by collisional excitation or by absorption of infrared radiation [29]. They can also lose energy through collisions with other atmospheric molecules or emission of infrared radiation. In the lower atmosphere, the "greenhouse effect" sees the emitted infrared radiation being quickly absorbed by other molecules due to the higher atmospheric densities. In the high atmosphere, any energy emitted is much more likely to be lost to lower altitudes or space due to the thinner atmosphere. This leads to a net cooling effect, reducing the temperature of the thermosphere as the CO_2 concentration increases. These temperature decreases lead to thermospheric contraction, causing a secular decrease in neutral atmospheric density at a given altitude [15].

A corresponding reduction in atmospheric drag has led to orbital lifetimes of satellites in the region increasing. Use of orbital data from the year 1967 onwards has allowed for historical observations of the density of the thermosphere, and has shown a long-term decrease in atmospheric density at LEO altitudes of around -1.7 to -7.2 % per decade (at 400 km) due to increasing carbon dioxide emissions. This, along with model studies of the historic trend, has been summarised in Table 1.

Solar activity is known to have a significant impact on thermospheric neutral densities, seeing an order of magnitude change in density between solar maxima and minima [8]. This is due to increased extreme ultraviolet emission heating the thermosphere during solar maxima, with the cycle having a roughly 11 year period. Solar activity also has an impact on the historic secular density reduction trend, with the largest percentage reductions seen during solar minima [5, 32].

If the historic density trends continue, there will be a larger cumulative reduction in density in the future. With debris model simulations running projections many decades, even centuries, into the future, secular density trends will have an important cumulative effect on simulated debris environments. Lewis et al. (2011) ran the Debris Analysis and Monitoring Architecture to the Geosynchronous Environment (DAMAGE) debris model with a fixed secular density trend of around -7.2% per decade, taken from Saunders 2011 [16, 28]. The impact on measures designed to reduce the amount of debris within the environment was investigated. Under these conditions, the benefits of Active Debris Removal (ADR) missions were cancelled out by the density trend, with further

Table 1. Summary of observations and models of the historic density trend at 400 km altitude.

Paper	Type	F10.7 (sfu)	Period	Density Trend (% per decade)
Keating et al., 2000 [12]	Observation	~75	1976, 1986, 1996	-5.04 ± 1.4
Marcos et al., 2005 [20]	Model	All	1970-2000	-1.7
Qian et al., 2006 [24]	Model	70	1970-2000	-2.5
Emmert et al., 2008 [3]	Observation	<75	1967-2007	-5.5 ± 1.4
Emmert et al., 2008 [3]	Observation	170 to 220	1967-2007	-2.1 ± 0.9
Saunders et al., 2011 [28]	Observation	<90	1970-2010	-7.2
Saunders et al., 2011 [28]	Observation	>90	1970-2010	-4.0
Emmert and Picone 2011 [4]	Observation	All	1967-2005	-1.94 ± 1.36
Emmert, 2015 [5]	Observation	60 to 75	1967-2005	-3.1 ± 1.6
Emmert, 2015 [5]	Observation	60 to 75	1967-2013	-7.2 ± 1.2
Solomon et al., 2015 [30]	Model	70	1996-2008	-4.9 or -6.8 [a]
Solomon et al., 2018 [31]	Model	70	1974-2003	-3.9
Solomon et al., 2019 [32]	Model	200	1974-2003	-1.7

[a] k_q, CO_2-O collisional deactivation rate, of $\sim 1.5 \times 10^{-12} cm^3 s^{-1}$ and $3.0 \times 10^{-12} cm^3 s^{-1}$

ADR missions required each year to regain those benefits. Within a mitigation-only scenario with widespread adoption of space debris guidelines, the density trend increased the LEO population growth rate by 74% over 70 years (2010-2080).

The Intergovernmental Panel on Climate Change (IPCC)'s Fifth Assessment Report (AR5) summarized research on possible future climates. Four Representative Concentration Pathways (RCPs) were created, with each providing a CO_2 concentration trajectory through to the year 2100 [10]. These are shown in Figure 1 and the number after each RCP refers to the radiative forcing in the year 2100 in W/m^2. These are not meant to be taken as predictions of the future, but rather to provide a limited number of baseline scenarios for CO_2 concentrations for modelling purposes and to allow comparison across different climate change studies.

2. MODEL DESCRIPTIONS

2.1. Atmospheric Model: CESM

The Community Earth System Model (CESM) from the National Center for Atmospheric Research (NCAR) can simulate the coupled Earth climate model, using individual models for each major system [9]. The Whole Atmosphere Community Climate Model - eXtended (WACCM-X) is used as part of CESM to numerically simulate the atmosphere from ground level up to around 500 km altitude [19]. WACCM-X has a resolution of 1.9° in latitude and 2.5° in longitude, giving a 96 by 144 grid. There are also 81 vertical pressure levels increasing in one-quarter scale height steps above 1 hPa.

Each pressure level has an associated, varying geopotential height, h, which can be converted to geometric altitude (equivalent to orbiting altitude), z, via

$$z = h\left(1 - \frac{h}{r_E}\right) \quad (1)$$

where r_E is the average radius of Earth. All values between the discrete pressure levels are found by 1-D monotonic cubic interpolation. The dynamic, physical, chemical, radiative, and electrodynamic processes are simulated within each grid cell to fully simulate the Earth's atmosphere. A detailed description can be found within Liu et al (2010) [19].

Within our WACCM-X simulations, only carbon dioxide and carbon monoxide concentrations are changed, as both exist in chemical equilibrium with each other within the thermosphere. Extra carbon from other greenhouse gases like methane (CH_4) could increase carbon dioxide concentrations through reactions. However, carbon dioxide and carbon monoxide alone account for 99.7% of the carbon within the thermosphere. Futhermore, the effect of changes in methane on the thermospheric density is expected to be much smaller than the effect of the increase in CO_2 concentration [26].

Nitric oxide (NO) also causes thermospheric cooling, particularly during solar maximum [21]. Nitrous oxide (N_2O) is a greenhouse gas which is predicted to have increased anthropogenic emission in the future, and can convert to NO in the upper atmosphere. However the large amount of nitrogen (N_2) in the lower atmosphere acts as a reservoir, keeping NO in the upper atmosphere at a stable level despite increasing N_2O emissions. This allows us to neglect N_2O emissions.

The Earth's magnetic field changes over time, affecting
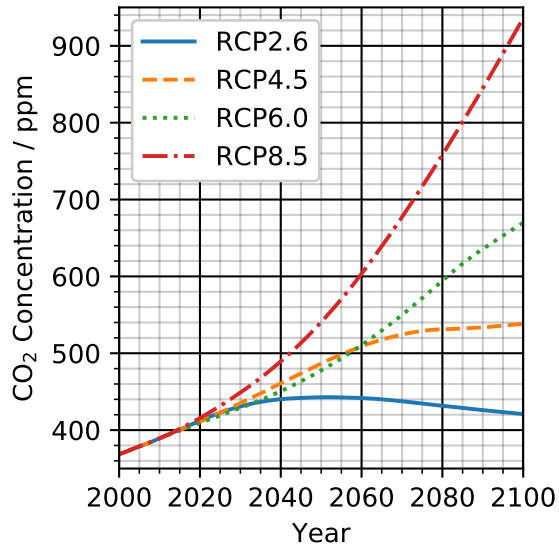
Figure 1. Representative Concentration Pathways (RCPs) published by the Intergovernmental Panel on Climate Change (IPCC) showing four possible scenarios for ground-level CO_2 concentrations through to the year 2100 [25].

the ionosphere and in turn the thermosphere [2]. Over the period 1908 to 2008, historic changes in the magnetic field contributed to cooling at 300 km, but the increasing CO_2 concentration dominated the combined thermospheric cooling. Even with the future change in magnetic field predicted to accelerate, the expected change up to the year 2065 will result in at most a 1 to 2% increase in neutral density. This is equivalent to a 0.2 to 0.4% per decade change over the 50 year period, an order of magnitude smaller than the -1.7 to -7.2 % per decade of historic CO_2 trends. Therefore the magnetic field in WACCM-X was held constant from the year 2000, following the International Geomagnetic Reference Field (IGRF-12) [33].

The fixed top-of-model pressure level in WACCM-X of 4×10^{-10} hPa reduces in altitude as the thermosphere cools at solar minimum, with this effect amplified by the thermospheric cooling of CO_2 emissions. At the highest modelled ground-level CO_2 and during solar minima, the maximum model altitude reaches as low as 280 km. Extrapolation was required to retrieve densities up to 500 km altitude in some cases. The function that best fit the atmospheric densities (ρ) at points above 175 km for all cases was calculated by

$$\rho(z) = bz^c \log(z + d) + f \qquad (2)$$

where b, c, d, and f are coefficients fit to the modelled density with non-linear squares for each latitude-longitude combination. The highest modelled altitudes of WACCM-X are dominated by atomic oxygen, but helium becomes the dominant chemical at around 700 km and

above. Once helium becomes dominant the extrapolation function would have to change. To verify the extrapolation method, it was applied to the empirical NRLMSISE-00 density model which does account for helium [23]. There was an increasing deviation with altitude, reaching an overestimate of on average 3% at 500 km. As will be seen in the results section, we have focused on relative differences in density rather than using the absolute densities of WACCM-X within our density model. As the overestimate was fairly consistent, it mostly cancelled out when taking the relative difference and so was deemed acceptable when used up to 500 km.

Global-mean annual-mean densities were calculated to remove the small latitude-longitude and seasonal dependence from the density reductions, first by averaging temporally, then over latitude (with cosine latitude weighting), and finally over longitude.

2.2. Fast Debris Model: BRAD

To quickly identify interesting scenarios arising due to the density reductions, a new statistical debris model has been created named the Binned Representative Atmospheric Decay (BRAD) debris model. It is summarised graphically in Figure 2, and has been based on the method used by the STochastic Analog Tool (STAT) debris model detailed in Rossi 1998 [27]. Objects are binned by semi-major axis (a), eccentricity (e), inclination (i) and mass (m). All calculations are then performed on a representative object at the centre of each bin, thereby reducing the number of calculations required.

The initial population is created from objects in a reference population obtained from ESA's Database and Information System Characterising Objects in Space (DISCOS) [6]. These are split up into the relevant bins. This is also done for launches, specifically over the January 1st 2005 to December 31st 2012 period. Launches are also binned temporally to match the model time step. These launches are repeated in a cyclical nature, albeit the initial start point is randomised to remove unintentional periodicity during Monte Carlo runs. Explosions are currently not handled by the model, but may be added in future.

Collisions are handled in a statistical manner using the algorithm described in Greenberg 1982 [7]. For each pair of bins, a probability of the orbits being close enough for a collision to occur can be calculated from the a, e, and i of the representative object of each bin. This is then multiplied by the probability that both objects are near the point of closest approach at the same time. Finally, a mean collision frequency between the representative objects is found by multiplying the above probability by the geometric cross section of the bodies. This procedure is computationally intensive but is constant for a given choice of bins, meaning it only has to be performed once and can then be retrieved each time for a specific choice of bins.

There is a correction to the Greenberg algorithm given in
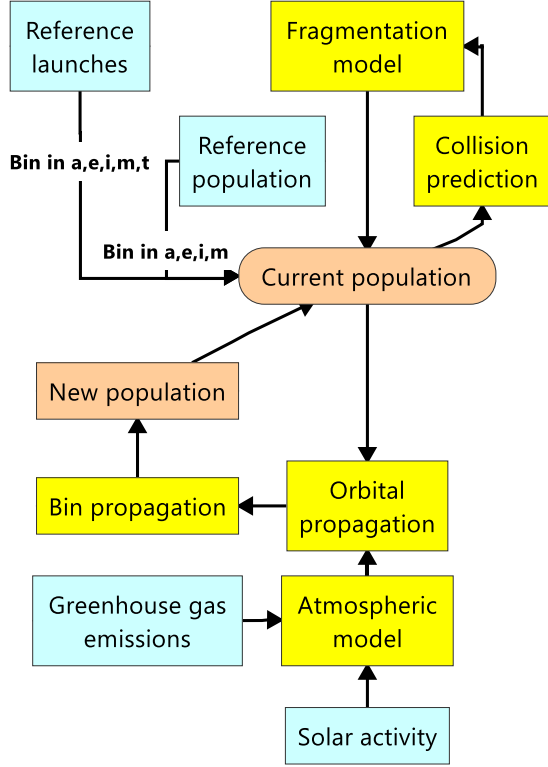
Figure 2. Map of the BRAD debris model. Blue denotes inputs, yellow the constituent models, and the orange the populations which can be output.

Bottke 1993 [1]. This is not currently implemented in the model but will be added in future versions. A comparison of the difference in collision probability is given in Table 2, along with the more widely used Cube algorithm. Both the Greenberg algorithm and the Bottke correction were originally created to calculate collision probabilities for asteroids (as reflected in Table 2) and make assumptions about the other orbital elements which have to be considered within the debris model. For example, both the longitude of ascending node and argument of perigee have to be uniformly distributed. Due to the binning method of the model and the long time steps, orbital perturbations will result in this uniform distribution requirement being met.

At each time step, the mean collision frequency for each bin pairing is used within a Poisson distribution and tested against a random number in a uniform distribution between 0 and 1 in order to give a random, integer number of collisions deemed to have occurred. Collisions are then simulated by sampling random masses from the two bins, and using the NASA standard breakup model to create a fragment distribution across mass bins [11, 22]. As the largest object carries the most momentum, for simplicity it is assumed the fragments reside in the same orbital (a,e,i) bin as the largest object. In reality a collision

Table 2. Comparison of the intrinsic collision probability (10^{-18} $km^{-2}yr^{-1}$) between Astrid and the given example bodies using the Greenberg (G), Greenberg with Bottke correction (G+B), and Cube algorithms [7, 1, 18]. Astrid's orbital elements are (a, e, i)=(2.75, 0.27, 0.28). Units of semi-major axis (a) are astronomical units, and inclination (i) is given in radians. Data taken from Liou 2003 [18].

Object	a	e	i	G	G+B	Cube
1948 EA	2.26	0.61	0.32	2.49	3.20	3.23
Apollo	1.48	0.56	0.11	3.24	3.60	3.77
Adonis	1.97	0.78	0.04	3.92	4.53	4.79
1950 DA	1.70	0.51	0.21	3.13	3.76	3.65
Encke	2.21	0.85	0.22	2.91	3.43	3.64
Brorsen	3.01	0.81	0.51	0.81	0.95	1.01

will result in a number of the fragments entering orbits corresponding to different (a, e, i) bins. The effect will be investigated in future work.

Orbital propagation is handled similarly to the Debris Cloud Propagator (DCP) of STAT and following the calculations of King-Hele 1987 [14]. The rate of change in semi-major axis is calculated by

$$\frac{da}{dt} = -\frac{a^2 \rho v^3 C_d (A/m)}{\mu} \qquad (3)$$

where ρ is the atmospheric density, v is the orbital velocity, C_d is the coefficient of drag (assumed uniformly to be 2.2), μ is the gravitation parameter of Earth, and A/m is the Area to mass ratio, which has been obtained from our binned mass through the Kessler and Cour-Palais 1978 [13] relation:

$$\frac{A}{m} = \left(\left(\frac{m}{62.0} \right)^{\left(\frac{1.0}{1.13} \right)} \right) \Big/ m \qquad (4)$$

The largest amount of drag (and hence semi-major axis change) occurs when an object's altitude is near to perigee. Therefore, King-Hele split the problem into three possible solutions, each depending on the proportion of the orbit spent close to perigee. These are:

- Near-circular ($2ae \leq \epsilon$)

- Almost-circular ($\epsilon < 2ae \leq 2H$)

- Elliptical ($2ae > 2H$)

where H is the atmospheric scale height and ϵ is a parameter defined as the minimum acceptable distance between apogee and perigee to class an orbit as near-circular. Following Rossi 1994, ϵ was set as 50 km.

The full equations for each solution can be found in King-Hele [14], but they each depend on the atmospheric density at perigee. We calculated this with the NRLMSISE-00 model [23], and then applied a scaling factor to account for the density reduction due to increases in CO_2 concentration. This scaling factor was calculated with use of the data we obtained from WACCM-X and is fully detailed in Section 3.1.

Once a change in semi-major axis is calculated by Equation 3, a change in eccentricity can be calculated by using a fixed perigee between the new and old orbit. A virtual bin of the same size as the original bin can be drawn around the propagated representative object. The number of objects in the original bin is then split by the proportion of the virtual bin overlapping the original bins. This is shown graphically in Figure 3. While this approach is fast, objects near the edge of the bin would propagate by a different amount to the central, representative object, skewing the original bin's shape. This is not accounted for in the model, but the effect can be minimised by using bins of a finer scale at the cost of model run time.
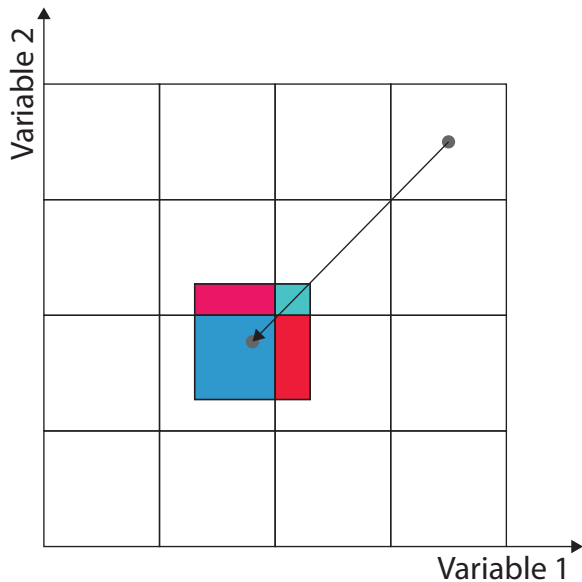
Figure 3. Graphical representation of bin propagation in two variables. A representative object is propagated, then the overlap of the bins (shown by differing colours) is calculated and the number of objects in the original bin is split proportionally into the bins.

3. RESULTS

3.1. Future Density Reductions

Three separate studies have been performed with WACCM-X which are summarised at 400 km altitude in Figure 4. The first two show the density reductions due to increasing ground-level CO_2 concentrations under low solar activity (F10.7 = 70 sfu), and under high solar activity (F10.7 = 200 sfu). The last looks at density reductions with a fixed CO_2 concentration of 639 ppm, but a varying F10.7. All three studies looked at the relative density compared to a reference year, taken as the year 2000.

Limited cluster computing time within which WACCM-X could be used, along with the run-time of 3 days per model year meant careful selection of repeats and data points had to be made. As a result no repeats have currently been made in the low solar activity study. However, 5 year-long repeats of each of the 8 modelled CO_2 values have been performed for high solar activity. The result was fairly consistent standard deviations of $\pm1.4\%$, with a maximum of $\pm2\%$. The F10.7 required repeats of the reference fixed-CO_2 year along with the the high-CO_2 year. Currently 2 repeats have been completed for each case for each of the 5 modelled F10.7 values.

In a similar way to the historic density trends, the greatest density reductions will occur during lower solar activity. Larger density reductions are seen with increasing altitude. In both the low and high solar activity studies, there is a bump in the data at around a ground-level CO_2 concentration of 480 and 500 ppm respectively. Density reductions do not decrease here as quickly with increasing CO_2 concentration compared to at other modelled CO_2 concentrations. Nothing in WACCM-X's input files or code has currently been found to explain this bump. However, the fact it has appeared within both studies is intriguing, suggesting a possibly unknown physical phenomenon preventing densities from decreasing as quickly, but which is then lost with further increasing CO_2 concentrations.

The three relative density studies have been combined to allow for a density reduction to be obtained for any given altitude (100 to 500 km), F10.7 (70 to 200 sfu), and CO_2 concentration (369 to 890 ppm). This required interpolation between data points and the assumption that a similar, scaled F10.7 dependence is seen at all ground-level CO_2 concentrations. Within the debris model, when altitudes or F10.7 occur which are outside the modelled range, the associated edge of the range is taken rather than extrapolating. The choice of a repeating solar cycle 24 limited this occurring for F10.7 values, and the capped density reduction for altitudes above 500 km reflected the decreases which would be seen above these altitudes without running into the helium dominance related extrapolation issues discussed in Section 2.1.

3.2. Debris Environment

The BRAD debris model described in Section 2.2 was used along with the density scaling factor to investigate the impact CO_2 emissions will have on the space debris environment. The binning was set up as described in Table 3 and the solar activity was set up to repeat solar cycle 24, as shown in Figure 5.

A Monte Carlo method was used to simulate the debris
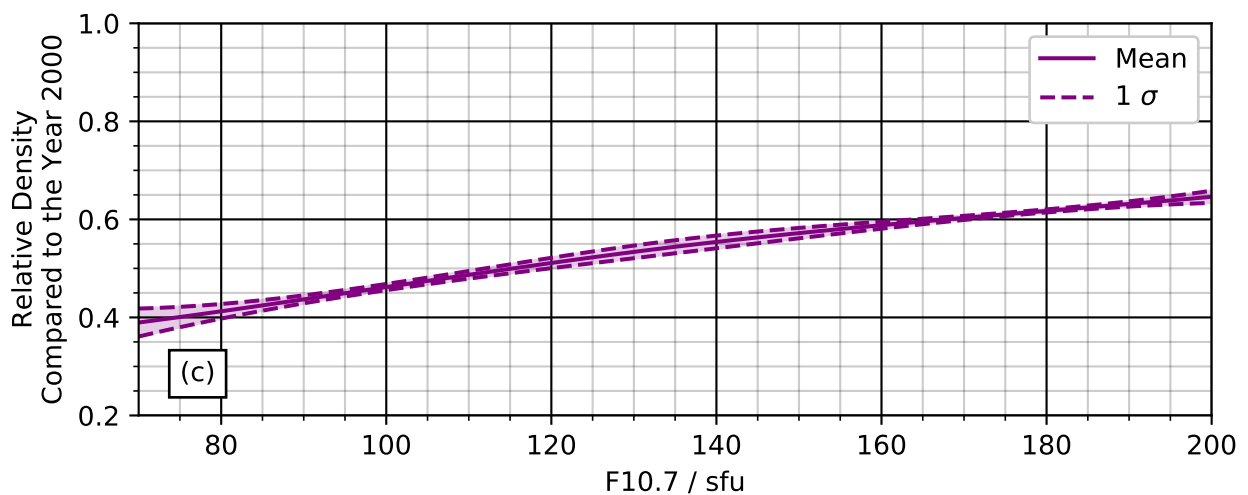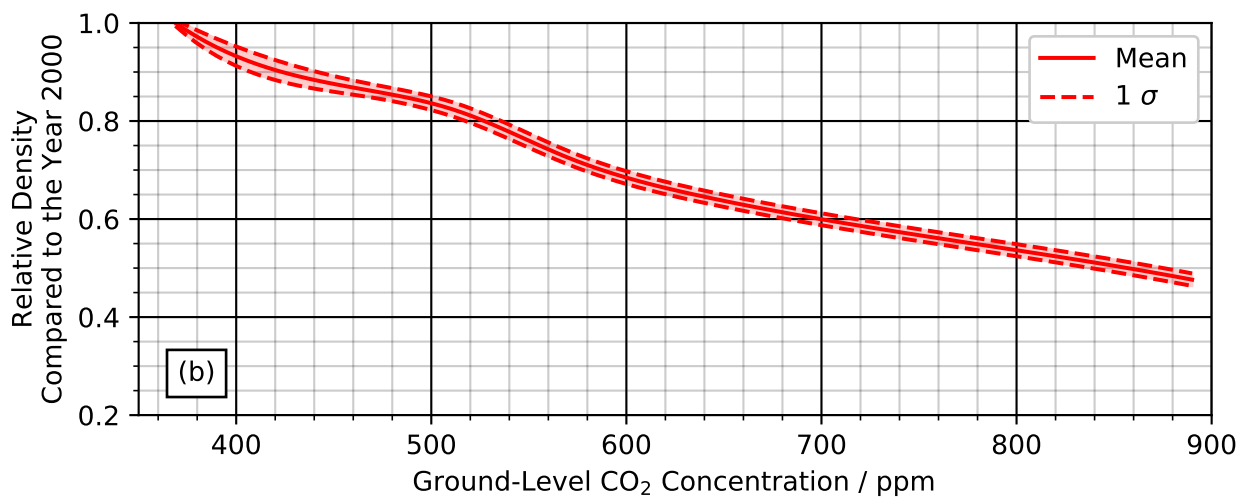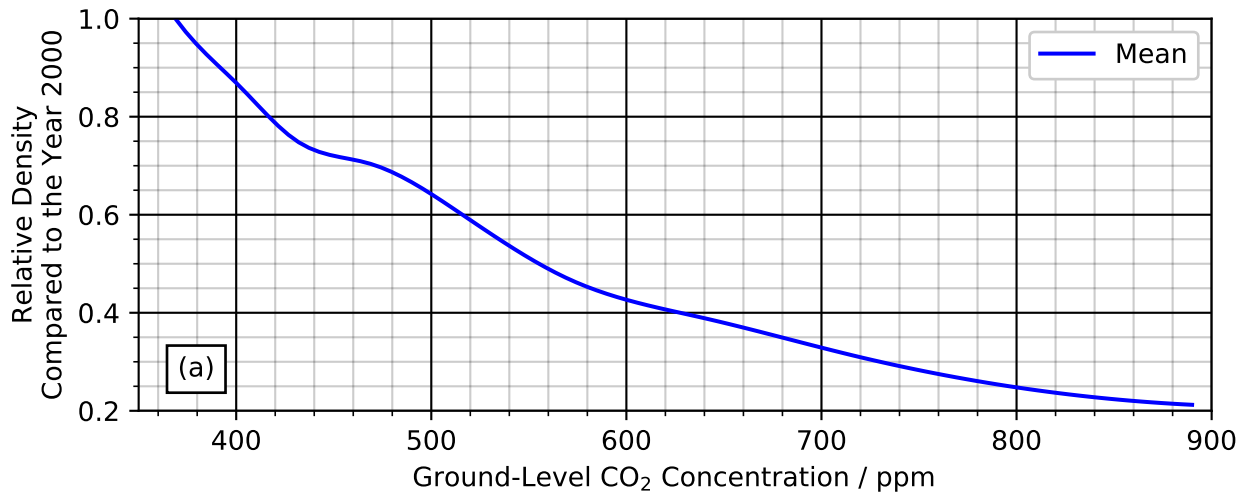
Figure 4. *Relative densities at 400 km altitude compared to the reference point of the year 2000 for (a) low solar activity with F10.7 = 70 sfu, (b) high solar activity with F10.7 = 200 sfu, and (c) for varying solar activity under a fixed ground-level CO_2 concentration of 639 ppm. No errors are given in (a) as currently only 1 model simulation has been performed for each data point. 5 simulations have been done for each data point in (b), and 2 for (c).*
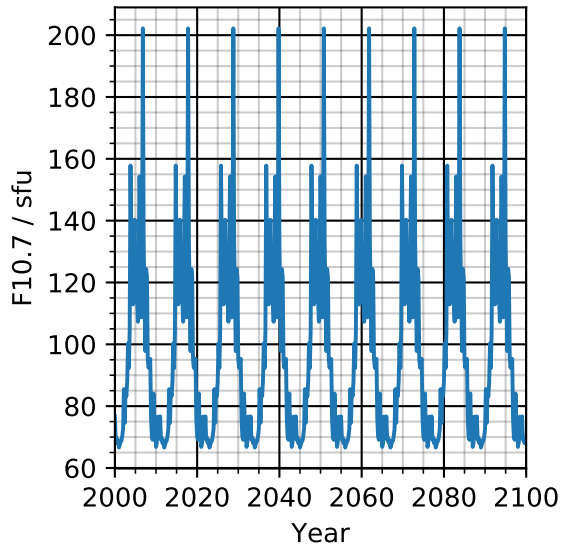
Figure 5. Solar activity used in the study, repeating solar cycle 24.

Figure 6. Debris environment Monte Carlo modelled within BRAD, plotting objects greater than 9.1 cm and with a perigee below 500 km. No density reductions applied so the atmospheric density is that of NRLMSISE-00 only.

Table 3. The bins used for orbital elements within BRAD.

	Minimum	Maximum	# Bins	Spread
a	6778 km	7578 km	16	Linear
e	0	0.05	16	Linear
i	0	$5\pi/8$	5	Linear
m	0.01 kg	3162 kg	13	Logarithmic

environment with BRAD, with 10 repeats made in each run. An initial simulation was made with no density reduction applied, and hence just using NRLMSISE-00 to obtain atmospheric densities. Figure 6 shows this scenario, showing only objects greater than 9.1 cm (closest complete bin to "trackable" 10 cm objects) and with a perigee below 500 km altitude.

Simulations of the debris environment under each of the RCP scenarios were then performed, with the results summarized in Figure 7. Only the density reductions due to increasing CO_2 concentrations were changed between each of the simulations. Even under RCP2.6 (Figure 7a), there is a substantial increase in the number of objects which is particularly noticeable from 2050 onwards, being over double the control scenario with no density reductions applied. The number of trackable objects below 500 km increases as the ground-level CO_2 concentration increases, with the largest changes as a result of RCP4.5, RCP6.0 and RCP8.5 occuring towards the end of the century. In each of these scenarios there is a cumulative effect of an increasing number of collisions combined with a further decreasing atmospheric density from increasing ground-level CO_2 concentrations.

The beneficial effect of density increasing by an order

of magnitude during solar maxima still removes the majority of objects below 500 km. However, this becomes less effective as the CO_2 concentration increases, with the density during solar maxima at 890 ppm reducing to a level closer to a density seen in present day solar minima. While the effect of the solar cycle can be easily seen in Figures 6 and 7(a, b), it becomes much less distinct in the latter part of the century under RCP6.0 of Figure 7(c). Within the RCP8.5 scenario, the solar activity periodicity is lost nearly completely and the number of objects increases exponentially as fewer objects are removed during solar maxima.

4. DISCUSSION

The Paris Agreement can be used to provide context to the possible CO_2 concentrations which will be seen in the future. The Emissions Gap Report from the United Nations Environment Programme (2019) [34] states that for a 50% probability of limiting global warming to 1.5°C (the target of the Paris Agreement), the carbon budget from 2018 onward is 580 GtCO2. Adding this to the 2017 globally averaged CO_2 concentration of 405.0 ppm gives a target of 480 ppm below which ground-level global warming is limited to 1.5°C [17]. This would limit density reductions at 400 km since the year 2000 to 15% at F10.7 = 200 sfu, and 31% at F10.7 = 70 sfu. The Paris Agreement target is independent of time and is reached in different years within the RCP4.5, RCP6.0, and RCP8.5 scenarios. RCP2.6 sees CO_2 concentrations stay below this CO_2 concentration. The Emissions Gap Report
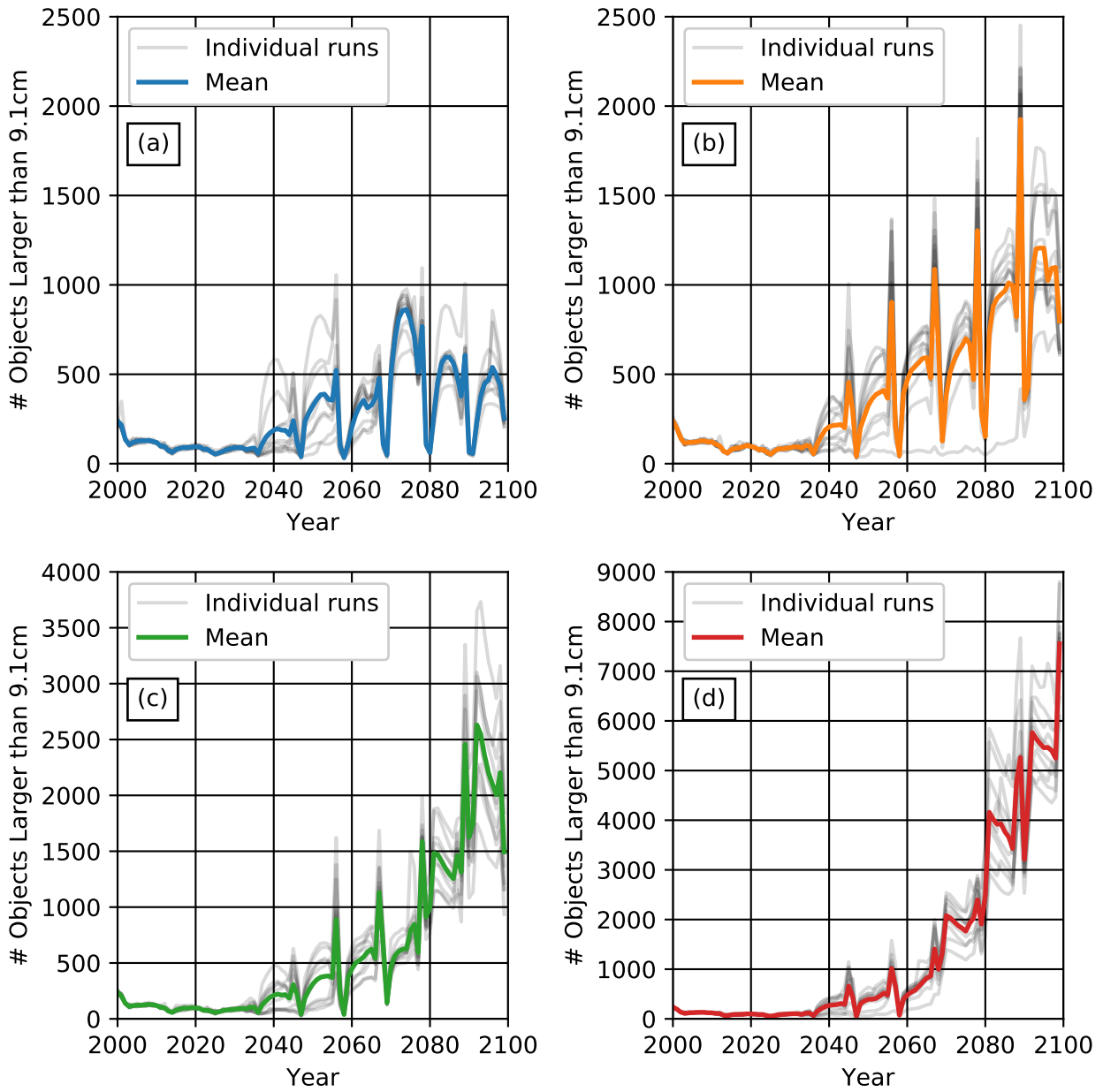
Figure 7. Debris environment Monte Carlo modelled within BRAD, plotting objects greater than 9.1 cm and with a perigee below 500 km. Similar colours denote the RCPs as in Figure 1, namely (a) RCP2.6, (b) RCP4.5, (c) RCP6.0, and (d) RCP8.5. While the y axes are the same in (a) and (b), they have been resized for (c) and (d) to make it easier to pick out the solar cycle effect.

also gives a prediction that under the current unconditional Nationally Determined Contributions (NDCs) and assuming a linear trajectory through to 2030, cumulative emissions are predicted to be around 510 $GtCO_2$ up until 2030. Therefore, the NDCs lead to a sharper short-term increase in CO_2 concentration than any of the RCPs suggest. As a result, the impact on the debris environment could be seen sooner than is shown in the results within Figure 7.

The BRAD model currently does not model the effects of large constellations of satellites, due in part to the assumptions made within the collision probability module. As a result, launches also followed a historic period before the larger constellation launches we see today. However, the density reductions shown in this work will have a substantial impact on the orbital lifetimes of constellations in LEO such as Starlink at 550 km and Project Kuiper at 600 km. More generally, the post-mission disposal of all space systems will need to take into account these density reductions when using atmospheric drag to passively remove satellites from orbit, whether through further lowering of the end-of-life perigee or re-entry technologies such as drag-sails.

5. CONCLUSIONS

While past work has identified the reductions in thermospheric density due to increasing CO_2 as a potential negative for the debris environment, little work has been done to quantify the impact it will have. This previous work also relied on empirical models of historic density trends based on satellite orbits, and so extrapolation into the future was not reliable. Our study has directly linked ground-level anthropogenic CO_2 emissions to changes in the thermosphere, allowing for use of RCPs to understand the future impact on the debris environment. We have shown that a very high CO_2 concentration of 890 ppm can lead to as much as a 80% reduction in thermospheric density since the 2000 at 400 km under lower solar activity. Lower CO_2 concentrations, like the 480 ppm of the Paris Agreement, lead to density reductions of 15 to 31% (high and low solar activity respectively). We've shown that even in the RCP2.6 scenario where CO_2 concentrations stay below 480 ppm, there is a doubling of the number of trackable objects below 500 km in the latter part of the century compared to if a density reduction is not taken into consideration. The rate of increase in the number of objects gets larger as the CO_2 concentration increases, in part due to solar maxima being less effective at decaying the orbits of LEO objects.

ACKNOWLEDGMENTS

REFERENCES

1. Bottke Jr, W. F., Greenberg, R. (1993). Asteroidal collision probabilities. *Geophysical Research Letters*, **20**(10), 879-881.

2. Cnossen, I. (2014). The importance of geomagnetic field changes versus rising CO2 levels for long-term change in the upper atmosphere. *Journal of Space Weather and Space Climate*, **4**, A18.

3. Emmert, J. T., Picone, J. M., Meier, R. R. (2008). Thermospheric global average density trends, 1967–2007, derived from orbits of 5000 near-Earth objects. *Geophysical Research Letters*, **35**(5).

4. Emmert, J. T., Picone, J. M. (2011). Statistical uncertainty of 1967–2005 thermospheric density trends derived from orbital drag. *Journal of Geophysical Research: Space Physics*, **116**(A2).

5. Emmert, J. T. (2015). Altitude and solar activity dependence of 1967–2005 thermospheric density trends derived from orbital drag. *Journal of Geophysical Research: Space Physics,* **120***(4), 2940-2950.*

6. *Flohrer, T., Lemmens, S., Bastida Virgili, B., Krag, H., Klinkrad, H., Parrilla, E., ... Pina, F. (2013, April). DISCOS-current status and future developments. In Proceedings of the 6th European Conference on Space Debris (pp. 1-7).*

7. *Greenberg, R. (1982). Orbital interactions-A new geometrical formalism. The Astronomical Journal,* **87***, 184-195.*

8. *Hathaway, D. H. (2015). The Solar Cycle, Living Reviews in Solar Physics,* **12***(1).*

9. *Hurrell, J. W., Holland, M. M., Gent, P. R., Ghan, S., Kay, J. E., Kushner, P. J., ... Marshall, S. (2013). The community earth system model: a framework for collaborative research. Bulletin of the American Meteorological Society,* **94***(9), 1339-1360.*

10. *IPCC, 2014: Climate Change 2014: Synthesis Report. Contribution of Working Groups I, II and III to the Fifth Assessment Report of the Intergovernmental Panel on Climate Change [Core Writing Team, R.K. Pachauri and L.A. Meyer (eds.)]. IPCC, Geneva, Switzerland, 151 pp.*

11. *Johnson, N. L., Krisko, P. H., Liou, J. C., Anz-Meador, P. D. (2001). NASA's new breakup model of EVOLVE 4.0. Advances in Space Research,* **28***(9), 1377-1384.*

12. Keating, G. M., Tolson, R. H., Bradford, M. S. (2000). Evidence of long term global decline in the Earth's thermospheric densities apparently related to anthropogenic effects. Geophysical Research Letters, **27**(10), 1523-1526.

13. Kessler, D. J., Cour-Palais, B. G. (1978). Collision frequency of artificial satellites: The creation of a debris belt. Journal of Geophysical Research: Space Physics, **83**(A6), 2637-2646.

14. King-Hele, D. (1987). Satellite orbits in an atmosphere. Theory and applications.

15. Laštovička, J., Akmaev, R. A., Beig, G., Bremer, J., Emmert, J. T. (2006), Global Change in the Upper Atmosphere. Science, **314**(5803), 1253-1254.

16. Lewis, H. G., Saunders, A., Swinerd, G., Newland, R. J. (2011). Effect of thermospheric contraction on remediation of the near-Earth space debris environment. Journal of Geophysical Research: Space Physics, **116**(A2).

17. Le Quéré, C., Andrew, R. M., Friedlingstein, P., Sitch, S., Hauck, J., Pongratz, J., ... Zheng, B. (2018). Global carbon budget 2018. Earth System Science Data, **10**(4), 2141-2194.

18. Liou, J. C., Kessler, D. J., Matney, M., Stansbery, G. (2003, March). A new approach to evaluate collision probabilities among asteroids, comets, and Kuiper Belt objects. Lunar and Planetary Science Conference (Paper No. 1823).

19. Liu, H. L., Foster, B. T., Hagan, M. E., McInerney, J. M., Maute, A., Qian, L., ... Oberheide, J. (2010). Thermosphere extension of the whole atmosphere community climate model. Journal of Geophysical Research: Space Physics, **115**(A12).

20. Marcos, F. A., Wise, J. O., Kendra, M. J., Grossbard, N. J., Bowman, B. R. (2005). Detection of a long-term decrease in thermospheric neutral density. Geophysical Research Letters, **32**(4).

21. Mlynczak, M. G., Hunt, L. A., Russell III, J. M., Marshall, B. T., Mertens, C. J., Thompson, R. E. (2016). The global infrared energy budget of the thermosphere from 1947 to 2016 and implications for solar variability. Geophysical research letters, **43**(23), 11934-11940.

22. NASA, Orbital Debris Quarterly News, October 2011. Volume 15, Issue 4.

23. Picone, J. M., Hedin, A. E., Drob, D. P., Aikin, A. C. (2002). NRLMSISE-00 empirical model of the atmosphere: Statistical comparisons and scientific issues. Journal of Geophysical Research: Space Physics, **107**(A12), SIA-15.

24. Qian, L., Roble, R. G., Solomon, S. C., Kane, T. J. (2006). Calculated and observed climate change in the thermosphere, and a prediction for solar cycle 24. Geophysical research letters, **33**(23).

25. RCP Database, 2009. Available at: http://www.iiasa.ac.at/web-apps/tnt/RcpDb

26. Roble, R. G., Dickinson, R. E. (1989). How will changes in carbon dioxide and methane modify the mean structure of the mesosphere and thermosphere?, Geophysical Research Letters, **16**(12), 1441-1444.

27. Rossi, A., Anselmo, L., Cordelli, A., Farinella, P., Pardini, C. (1998). Modelling the evolution of the space debris population. Planetary and Space Science, **46**(11-12), 1583-1596.

28. Saunders, A., Lewis, H., Swinerd, G. (2011). Further evidence of long-term thermospheric density change using a new method of satellite ballistic coefficient estimation. Journal of Geophysical Research: Space Physics, **116**(A2).

29. Sharma, R. D., Roble, R. G. (2002). Cooling mechanisms of the planetary thermospheres: The key role of O atom vibrational excitation of CO_2 and NO, ChemPhysChem, **3**(10), 841–843.

30. Solomon, S. C., Qian, L., Roble, R. G. (2015). New 3-D simulations of climate change in the thermosphere. Journal of Geophysical Research: Space Physics, **120**(3), 2183-2193.

31. Solomon, S. C., Liu, H. L., Marsh, D. R., McInerney, J. M., Qian, L., Vitt, F. M. (2018). Whole atmosphere simulation of anthropogenic climate change. Geophysical Research Letters, **45**(3), 1567-1576.

32. Solomon, S. C., Liu, H. L., Marsh, D. R., McInerney, J. M., Qian, L., Vitt, F. M. (2019). Whole atmosphere climate change: Dependence on solar activity. Journal of Geophysical Research: Space Physics, **124**(5), 3799-3809.

33. Thébault, E., Finlay, C. C., Beggan, C. D., Alken, P., Aubert, J., Barrois, O., ... Zvereva, T. (2015). International geomagnetic reference field: the 12th generation. Earth, Planets and Space, **67**(1), 1-19.

34. United Nations Environment Programme (2019). Emissions Gap Report 2019. UNEP, Nairobi.